



OPEN

# Solution-processed $\text{NO}_2$ gas sensor based on poly(3-hexylthiophene)-doped PbS quantum dots operable at room temperature

JinBeom Kwon<sup>1,3</sup>, Yuntae Ha<sup>1,2,3</sup>, Suji Choi<sup>1,2</sup>, Dong Geon Jung<sup>1</sup>, Hee kyung An<sup>1</sup>, Seong Ho Kong<sup>2</sup>✉ & Daewoong Jung<sup>1</sup>✉

The global industrial development and increase in the number of transportation vehicles, such as automobiles and ships, have led to a steady increase in the issues related to greenhouse gas emissions.  $\text{NO}_2$  is a greenhouse gas emitted in large quantities from automobiles and factories, and its emission is unavoidable in the modern world. Therefore, a sensor capable of precise detection of  $\text{NO}_2$  is required. The most commonly reported types of  $\text{NO}_2$  sensors are those based on metal oxides. However, their operation at room temperature is impossible owing to their high-temperature operating characteristics, and therefore, a heater must be designed inside or installed outside the sensor for heating. Meanwhile,  $\text{NO}_2$  sensors based on PbS quantum dots (QDs) are advantageous as they can operate at room temperature and can be easily manufactured through a solution process rather than a complicated semiconductor process. Herein, a  $\text{NO}_2$  sensor was fabricated by doping PbS QDs with poly(3-hexylthiophene) (P3HT). The as-developed sensor exhibited high responsivity to 100–0.4-ppm  $\text{NO}_2$  gas with a resolution of 200 ppb owing to the stability of the thin film and high hole mobility of P3HT.

**Keywords** Gas sensor,  $\text{NO}_2$ , PbS QDs, P3HT

Recently, owing to the worldwide industrial development and the increase in the number of transportation vehicles, such as automobiles and ships, concerns of global warming caused by greenhouse gases have been steadily increasing. To resolve the issue of global warming, the European Union have adopted the Paris Agreement to curb the increasing temperature by limiting greenhouse gas emissions in 195 countries<sup>1</sup>. In the modern society,  $\text{NO}_2$ , which is a greenhouse gas, is inevitably emitted in large quantities from automobile exhausts and industrial sites.  $\text{NO}_2$  gas has severe adverse effects on the environment and human health.  $\text{NO}_2$  exposure to the human body causes serious lung-related diseases, and a high degree of  $\text{NO}_2$  exposure increases the probability of Alzheimer's disease<sup>2</sup>. Therefore, the development of a sensor capable of the precise detection of  $\text{NO}_2$  gas is required. Among the various types of  $\text{NO}_2$  sensors, metal oxide-based sensors are the most common<sup>3–7</sup>. However, their operation at room temperature is impractical because of their high-temperature operating characteristics. Therefore, a heater must be designed inside or installed outside the sensor for heating. This complicates the manufacturing process and increases the production cost and power consumption. Furthermore, the selectivity of these sensors is low owing to their high responsivity to other gases in addition to  $\text{NO}_2$ . Moreover, a major disadvantage of the metal oxide-based sensors is their low stability in a high-humidity environment. In contrast,  $\text{NO}_2$  gas sensors based on PbS quantum dots (QDs) have the advantages of being operable at room temperature and easily manufacturable through a solution process rather than the complicated semiconductor process<sup>8–11</sup>. Additionally, QDs can be easily synthesized through the colloidal method, and their particle size can be facilely controlled by adjusting the precursor concentration and synthesis time. These characteristics are advantageous because the sensitivity

<sup>1</sup>Advanced Mobility System Group, Korea Institute of Industrial Technology (KITECH), Daegu 42994, Republic of Korea. <sup>2</sup>School of Electronic and Electrical Engineering, Kyungpook National University, Daegu 41566, Republic of Korea. <sup>3</sup>These authors contributed equally: JinBeom Kwon and Yuntae Ha. ✉email: shkong@knu.ac.kr; dwjung@kitech.re.kr

can be improved through surface area optimization during thin-film formation. Poly(3-hexylthiophene) (P3HT) is a conductive polymer that possesses a high hole mobility and can improve the uniformity and quality during thin-film formation, which are advantageous. Therefore, it is widely used in optical devices, such as light-emitting diodes and solar cells<sup>12–16</sup>. In this study, a NO<sub>2</sub> sensor was fabricated by doping P3HT with PbS QDs. P3HT improves the adhesion between the PbS QDs and substrate, forming a thin film with only one layer. Moreover, it increases the reaction speed and sensitivity of the sensor by improving the mobility of the holes inside the device when reacting with NO<sub>2</sub><sup>17–19</sup>. An analysis of the response of the fabricated sensor to NO<sub>2</sub> gas revealed that PbS QDs doped with P3HT at a ratio of 1:1 could detect 100–0.4 ppm of NO<sub>2</sub> with a resolution of 200 ppb at a wavelength of 905 nm.

## Methods

### Synthesis of colloidal PbS QDs

The wavelength band of QDs can be tuned by controlling the nanoparticle (NP) size based on quantum confinement, which is a physical phenomenon wherein the bandgap changes as a function of the NP size. Herein, we synthesized PbS QDs possessing wavelengths of 905, 1210, and 1392 nm using a colloidal method<sup>20–23</sup>. A colloid is a dispersion of particles that are larger than a molecule or ion and possess at least one dimension between approximately 1 and 10 nm in a gas or liquid. Figure 1 demonstrates the synthesis method of PbS QDs. Briefly, a mixture sulfur (0.36 mmol; 99.998%; Sigma-Aldrich) and oleylamine (OLA, 0.24 mL; 70%; Sigma-Aldrich) was stirred at room temperature for 30 min. Thereafter, a mixture PbCl<sub>2</sub> (1–3 mmol; 99.999%; Sigma-Aldrich) and OLA (5 mL) was placed in a three-hole flask and stirred at room temperature under a N<sub>2</sub> gas (99.999%; ocean) airflow (Heat gas Inc.) for 30 min. Subsequently, the PbCl<sub>2</sub>–OLA mixture was heated at 160 °C for 1 h, followed by vacuum degassing at 120 °C for 20 min. Afterward, the S storage solution and trioxyethylphosphine (225 µL; 97%, Sigma-Aldrich) were rapidly injected into a three-neck flask under a N<sub>2</sub> gas flow. After allowing the chemical reaction to proceed at 100 °C for 1–360 min, the three-neck flask was cooled to room temperature. The synthesized PbS QD mixture was cleaned by injecting it with ethanol (20 mL; 99%; Sigma-Aldrich) and centrifuging at 4000 rpm for 10 min (FLETA-5, Hanil Scientific Inc.). Finally, the purified PbS QDs were dispersed in toluene (99.8%; Sigma-Aldrich), which is a nonpolar solvent, at 20 mg/mL. To synthesize P3HT-doped PbS QDs, P3HT was injected into the PbS QD solution and dispersed at weight ratios of 1:1, 1:0.5, 1:0.25, and 1:2<sup>24,25</sup>.

### Device fabrication

To maximize the uniformity of the thin-film formation of QDs and their reactivity with gas, the ratio between P3HT and PbS QDs was optimized. For ratio optimization, devices were fabricated and evaluated with QDs possessing an absorption wavelength of 900 nm. The ratios between PbS QDs and P3HT were fixed at 1:1, 1:0.5, and 1:0.25. Notably, when the ratio was 1:2 or higher, thin-film formation was difficult owing to gelation. Additionally, to optimize the reactivity according to the particle size of the QDs, devices were fabricated using QDs with the absorption wavelengths of 905, 1210, and 1392 nm. The film was deposited via spin casting onto pre-cleaned gold interdigitated electrodes (IDEs) on an oxide-coated silicon substrate. Figure 2 presents a schematic of the deposition procedure. Briefly, PbS QDs–P3HT mixed solutions (100 µL) were coated onto the substrate through spin casting (LT-MS 200, LTS); thereafter, annealing was performed in a vacuum oven (OV-11, JEIO Tech) at 95 °C for 30 min. The fabrication process is summarized in Fig. 2. In this study, devices with different P3HT ratios were fabricated to investigate the effects of this parameter on the sensor response. Several devices (>40) were fabricated to account for the statistical variations in the sensor performance.

### Sensor measurement system

To characterize the fabricated device, its current characteristics were measured as a function of the gas concentration. The measurement was performed using a gas sensor measurement system comprising a gas chamber, mass flow controller (MFC), and source meter unit (Fig. 3). Using the MFC controller, the NO<sub>2</sub> gas concentration was adjusted by combining 200 and 20 ppm of air-balanced NO<sub>2</sub> gas with air at a flow rate of 1000 sccm. Gas reaction

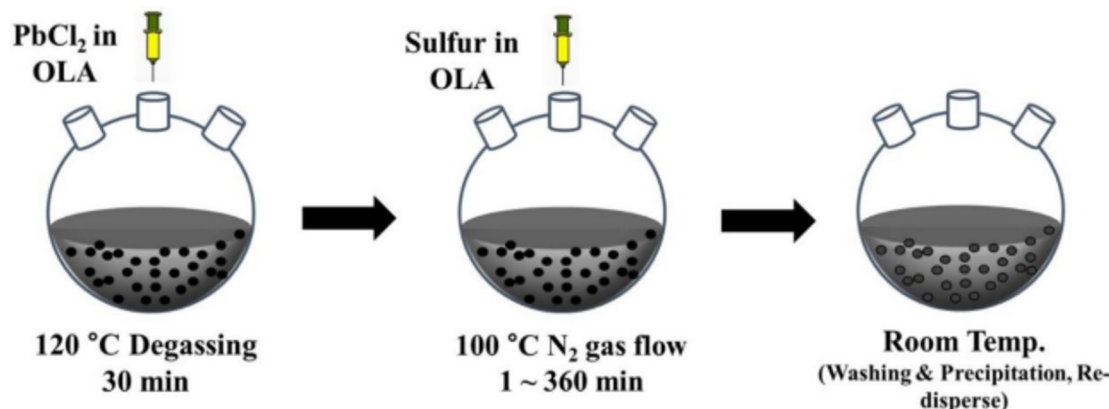


**Fig. 1.** Schematic of the synthesis of PbS QDs.

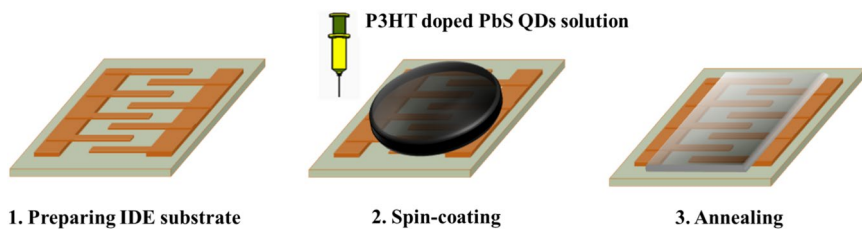


**Fig. 2.** Schematic illustrating the fabrication of a PbS QD-based  $\text{NO}_2$  gas sensor.

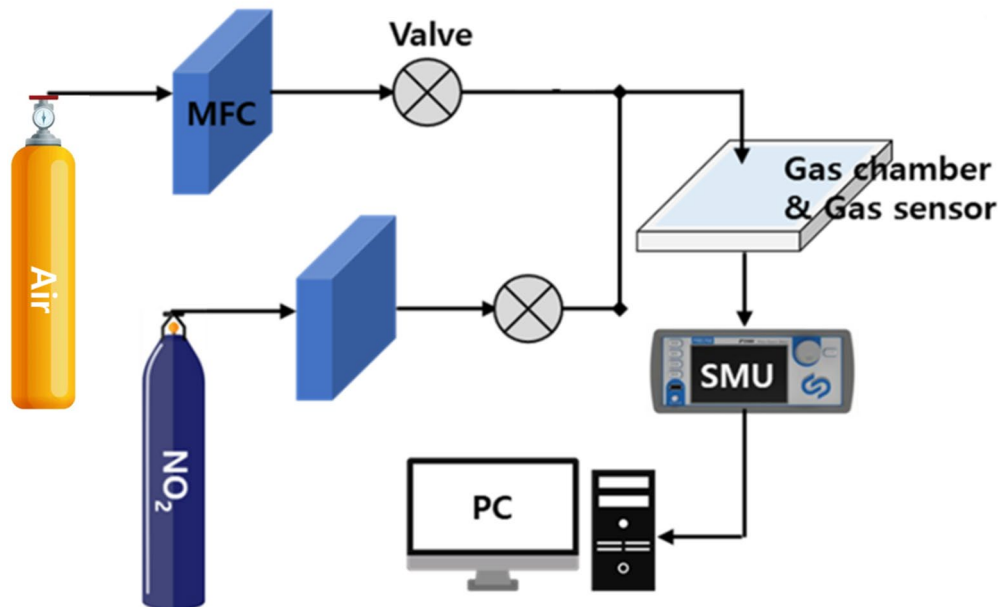


**Fig. 3.** Schematic of the  $\text{NO}_2$  gas measurement system of the fabricated sensor.

and recovery were repeatedly conducted for 10 min each, and air ( $\text{N}_2$ : 78%;  $\text{O}_2$ : 21%) was used as the recovery gas. All sensor measurements were conducted at room temperature (25 °C), except for the temperature-based experiments. The measured data were analyzed using origin 2023b (Origin lab, [www.originlab.com](http://www.originlab.com)).

## Results and discussion

### Characteristics of the synthesized PbS QDs

Absorbance, X-ray diffraction (XRD), and transmission electron microscopy (TEM) analyses of the synthesized QDs were conducted to evaluate their characteristics and successful synthesis. The obtained results are presented in Fig. 4. The absorbance spectra of the synthesized QDs presented in Fig. 4a reveals peaks at 905, 1210, and 1392 nm, indicating a high absorbance in the infrared region. The wavelength band of QDs changes depending on the particle size owing to quantum confinement. Based on quantum confinement, when the size of a particle is smaller than the Bohr radius, the instability increases with decreasing particle size, whereas the bandgap of the particle increases. Based on Eq. (1), the bandgap and wavelength band are inversely proportional. Because the band gap and particle size are inversely proportional, the wavelength band and size of the QDs are directly proportional.

$$Eg(\text{eV}) = \frac{1240}{\lambda} \quad (1)$$

Furthermore, to determine the crystal structure and particle size of PbS QDs, XRD (D8-DISCOVER, Bruker AXS) analysis was performed, and the results are displayed in Fig. 4b. For XRD analysis, the PbS QD sample solutions (10 mg/mL) were spin-coated on a 10 × 10-mm<sup>2</sup> glass substrate at 1000 rpm for 30 s, followed by annealing at 110 °C for 30 min. The lattice peaks in the patterns of all the synthesized PbS QDs were in conformance with those reported for PbS QDs in literature, and the peak intensity of (220) reflection increased with increasing particle size<sup>26</sup>. In addition, the peaks of P3HT were confirmed at approximately 23.6° and 37° only in P3HT-doped QDs (JCPDS File no-4S-2040)<sup>27</sup>. The crystallite size of PbS QDs (1210 nm) was calculated from the XRD results using the Scherrer equation<sup>28</sup>.

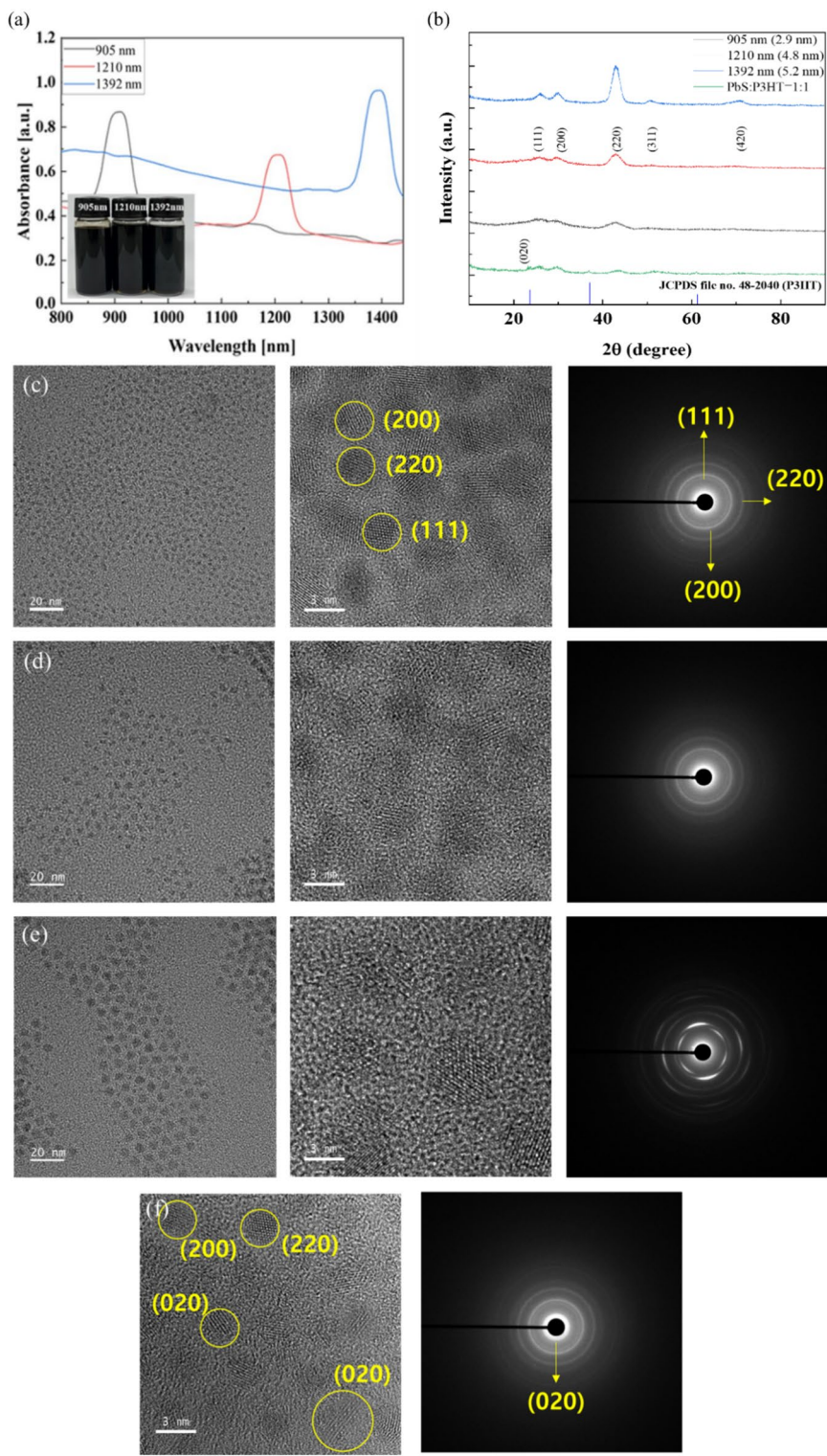


**Fig. 4.** Measured results: (a) Absorbance properties; (b) XRD patterns; (c), (d), and (e) TEM images of the synthesized QDs.

$$D_{hkl}(\text{nm}) = (K * \lambda) / \beta \cos \theta. \quad (2)$$

Here,  $K$  is the Scherrer constant,  $\lambda$  is the wavelength of X-ray,  $b$  is the maximum half width in radians, and  $q$  is the half-value between the incident angle and scattered X-ray wavelength vector. Gaussian fitting was performed to measure the theta value and full width at half maximum (FWHM), and the peaks with a precise fit were selected.  $K$  is 0.94 for a spherical crystallite possessing cubic symmetry with  $q = 15.1$ ,  $\text{FWHM} = 1.74$ , and

$\lambda = 0.15418$  nm, which is the wavelength of Cu K-alpha X-rays. The size of PbS QDs calculated using the Scherrer equation was 4.94 nm. Additionally, the TEM images presented in Fig. 4c-e reveal that the particle sizes of the synthesized PbS QDs with the absorption wavelengths of 905, 1210, and 1392 nm are 2.9, 4.8, and 5.2 nm, respectively. The lattice space and selected area electron diffraction (SAED) of PbS QDs were analyzed through TEM image, and the lattice space and SAED of (111), (220), and (200) were confirmed. These results confirm the successful synthesis of QDs. In addition, the lattice space and SAED of (020) were confirmed only in P3HT-doped PbS QDs, which confirmed that they were P3HT doped.

### Performance of the $\text{NO}_2$ gas sensor

To determine the optimal P3HT doping ratio, PbS QDs with an absorbance wavelength of 905 nm were used to evaluate the reactivity of various P3HT concentrations. Figure 5a-d illustrate the real-time responsivity of PbS QDs with the absorbance wavelength of 905 nm based on the P3HT doping ratio under the conditions of 100–20 ppm  $\text{NO}_2$  gas. Responsivity was calculated using Eq. (3).

$$\text{Response} = \frac{I_1 - I_0}{I_0} = \frac{\Delta I}{I_0} \quad (3)$$

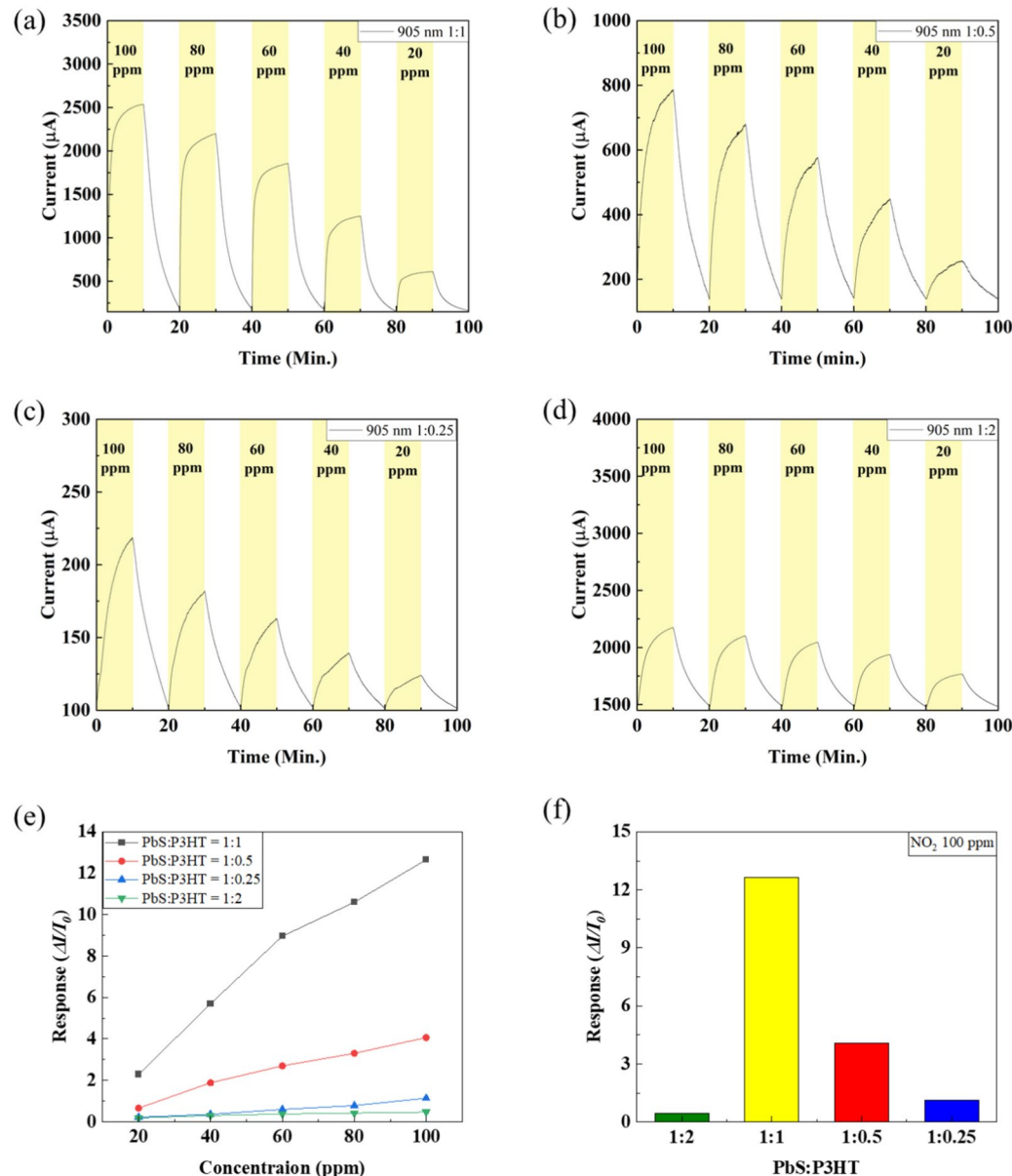


**Fig. 5.** (a-d) Current, (e) response characteristics based on the P3HT ratio at a  $\text{NO}_2$  gas concentration of 100–20-ppm and (f) responses at 100-ppm  $\text{NO}_2$  gas.

Here,  $I_0$  is the initial current of the sensor measured in air and  $I_1$  is the current when the sensor is exposed to the target gas.

The highest and lowest response values were obtained when the ratio of PbS QDs to P3HT was 1:1 and 1:2, respectively. Figure 5e depicts the reactivity as a function of the  $\text{NO}_2$  gas concentration for different P3HT doping ratios, and Fig. 5f presents the reactivity according on the P3HT doping concentration under the condition of 100 ppm  $\text{NO}_2$  gas. The results confirm that the response at the ratio of 1:1 is approximately 40 times higher than that at the ratio of 1:2, and therefore, the former is adopted as the optimal P3HT doping ratio. When the ratio is 1:1, a thin film is stably formed; PbS QDs are uniformly deposited; sufficient reaction occurs upon gas contact. However, when the ratio is 1:2, P3HT is highly dominant. Consequently, the thin film is produced in a gel form, and the number of PbS QDs in contact with  $\text{NO}_2$  gas decreases. Therefore, the QD thin films with absorbance at 905, 1210, and 1392 nm were fabricated at an optimized ratio of 1:1 for the subsequent experiments.

Next, the reactivity was measured as a function of the  $\text{NO}_2$  gas concentration in real time for the QDs with various wavelengths, and the results are presented in Fig. 6a-d. The gas concentration was varied from 20 to 1 ppm in 5-ppm decrements, and both the reaction and recovery times were maintained at 10 min. The measurements at 20-ppm  $\text{NO}_2$  revealed that the device comprised 905-nm PbS QDs exhibited the highest response of 2.06, which is ~ 2.1 times higher than that obtained for 1210-nm PbS QDs possessing a responsivity of 0.98.

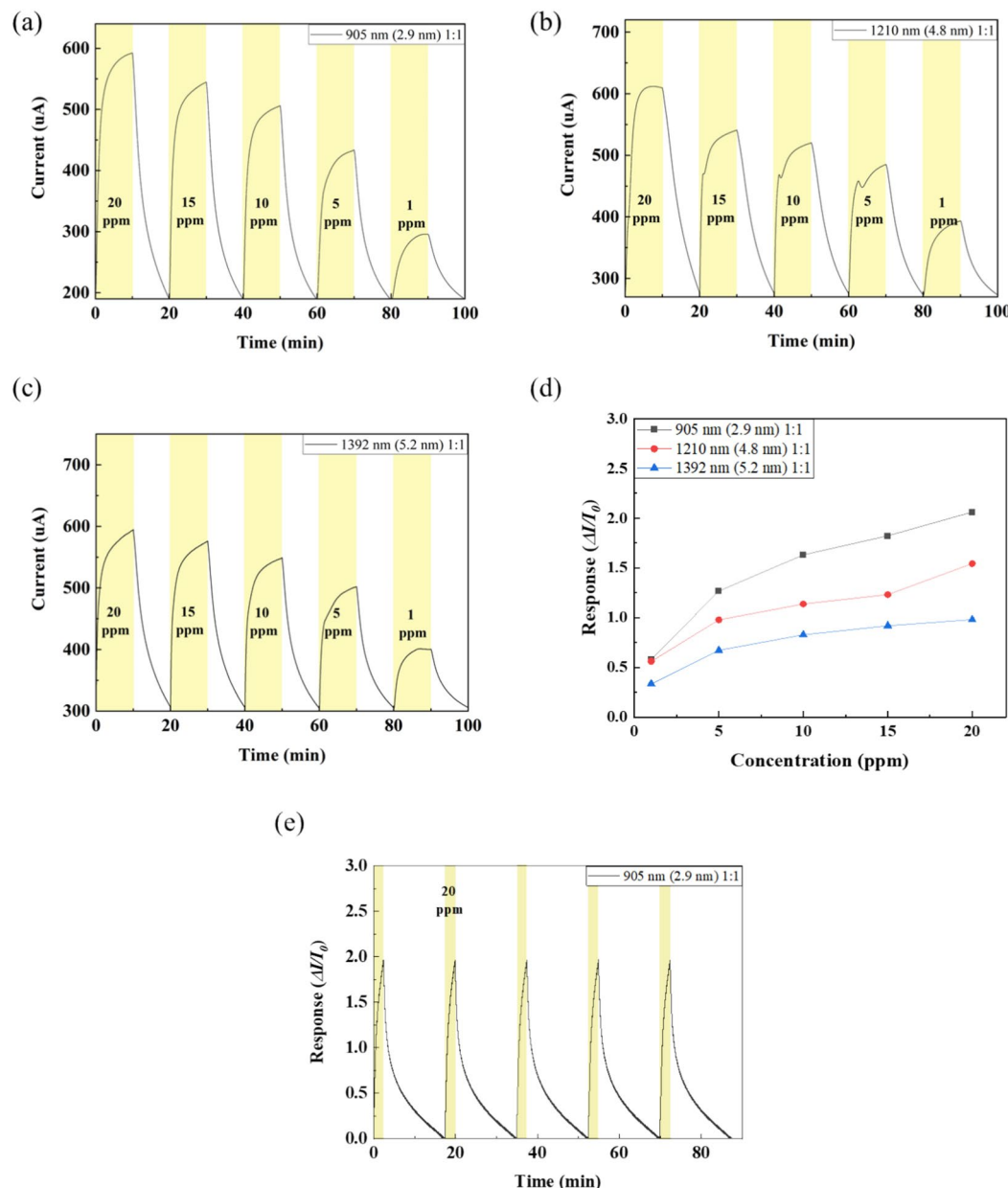


**Fig. 6.** (a-d) Current characteristics based on the size of PbS QDs at a  $\text{NO}_2$  gas concentration of 20–1 ppm, and (e) repeatability graph of the 2.9-nm PbS QD-based sensor at 25 °C.

The core size of PbS QDs with a wavelength of 905 nm is 2.9 nm, which is smaller than those of the QDs with the wavelengths of 1210 (core size = 4.8 nm) and 1392 nm (core size = 5.2 nm). Additionally, a repeatability test was conducted with the response and recovery times of 200 and 800 s, respectively, at the  $\text{NO}_2$  gas concentration of 20 ppm to confirm the reliability of the fabricated sensor (Fig. 6e). The error in the response measurements repeated for five times was within 1%. The size of the PbS QDs with a wavelength of 905 nm is 3.9 nm, and therefore, a uniform thin film with a large surface area can be obtained compared with that formed using large PbS QDs. The atomic force microscopy (AFM) results presented in Fig. 7 confirm that the thin film formed from 905 nm PbS QDs exhibits the smallest height deviation among the tested PbS QD thin films. Therefore, the area of reaction with gas is the largest for the 905-nm PbS QDs, and the quality of the thin film is high, resulting in stable electrical characteristics. Consequently, a higher reactivity is expected when the size of the synthesized QDs is smaller. However, the minimum limit of the wavelength range of PbS QDs is 905 nm, which renders the fabrication of small QDs impossible.

To evaluate the low-concentration  $\text{NO}_2$  gas sensing characteristics, the fabricated devices were evaluated at  $\text{NO}_2$  gas concentrations of 1–400 ppb with a resolution of 200 ppb. Figure 8 reveals that the device fabricated using 905-nm QDs exhibits the highest reactivity. At a concentration of 400 ppb  $\text{NO}_2$ , the response values of the device were 0.21, 0.19, and 0.13, respectively. Therefore, the  $\text{NO}_2$  gas detection limit of the fabricated device was confirmed as 400 ppb. Furthermore, the repeatability of low-concentration  $\text{NO}_2$  gas sensing was tested. From Fig. 8e at a concentration of 1 ppm, the error in the measurement of responsivity is within 1%, which is the same as that achieved at high concentrations. Metal oxide-based  $\text{NO}_2$  gas sensors have high sensitivity, but they operate at high temperatures and require high-temperature calcination processes or complicated semiconductor processes. The proposed sensor has the advantages of being easy to mass-produce through a solution process, not requiring a high-temperature calcination process or semiconductor process and being able to detect with good sensitivity at room temperature. As can be seen in Fig. 9, when heated to 100 °C, it has a four times higher response, which is higher than that of other studies. To compare the response with the reference sensors presented in the Table 1, the sensor response at 10 ppm in each paper was compared. Compared to not only the PbS QDs-based sensor but also the metal oxide-based sensor, the proposed sensor was confirmed to have the good response. In addition, the widest range of measured concentration characteristics was confirmed, and the LOD was also confirmed to be excellent at 70 ppb<sup>10,29–36</sup>. There are previous studies that show high sensitivity in a relatively small  $\text{NO}_2$  gas detection range of ppb level, and they are mainly studied for application in the atmospheric environment or respiratory/bio fields<sup>36</sup>. However, since the emission sources such as power plants, factories, and automobile exhaust gases emit more than several tens of ppm of  $\text{NO}_2$  gas due to fossil fuel combustion, such prior research has limitations in industrial use due to its small detection range. In addition, according to the regulations of the Occupational Safety and Health Administration (OSHA), if the workers at the industrial sites are exposed to  $\text{NO}_2$  gas above 5 ppm, it can be dangerous to the workers and requires warning and evacuation. Therefore, the sensor proposed in this study can not only secure the safety of the workers by detecting  $\text{NO}_2$

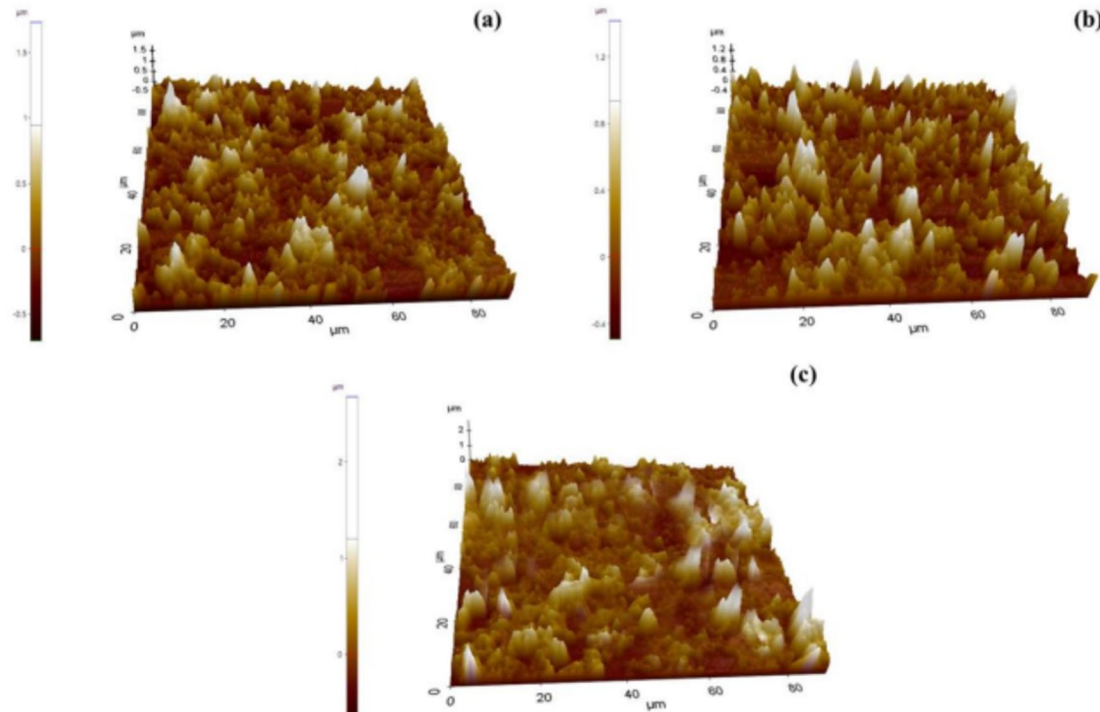


**Fig. 7.** Surface AFM measurement results for the fabricated sensors based on the size of PbS QDs: (a) 2.9, (b) 4.8, and (c) 5.2 nm.

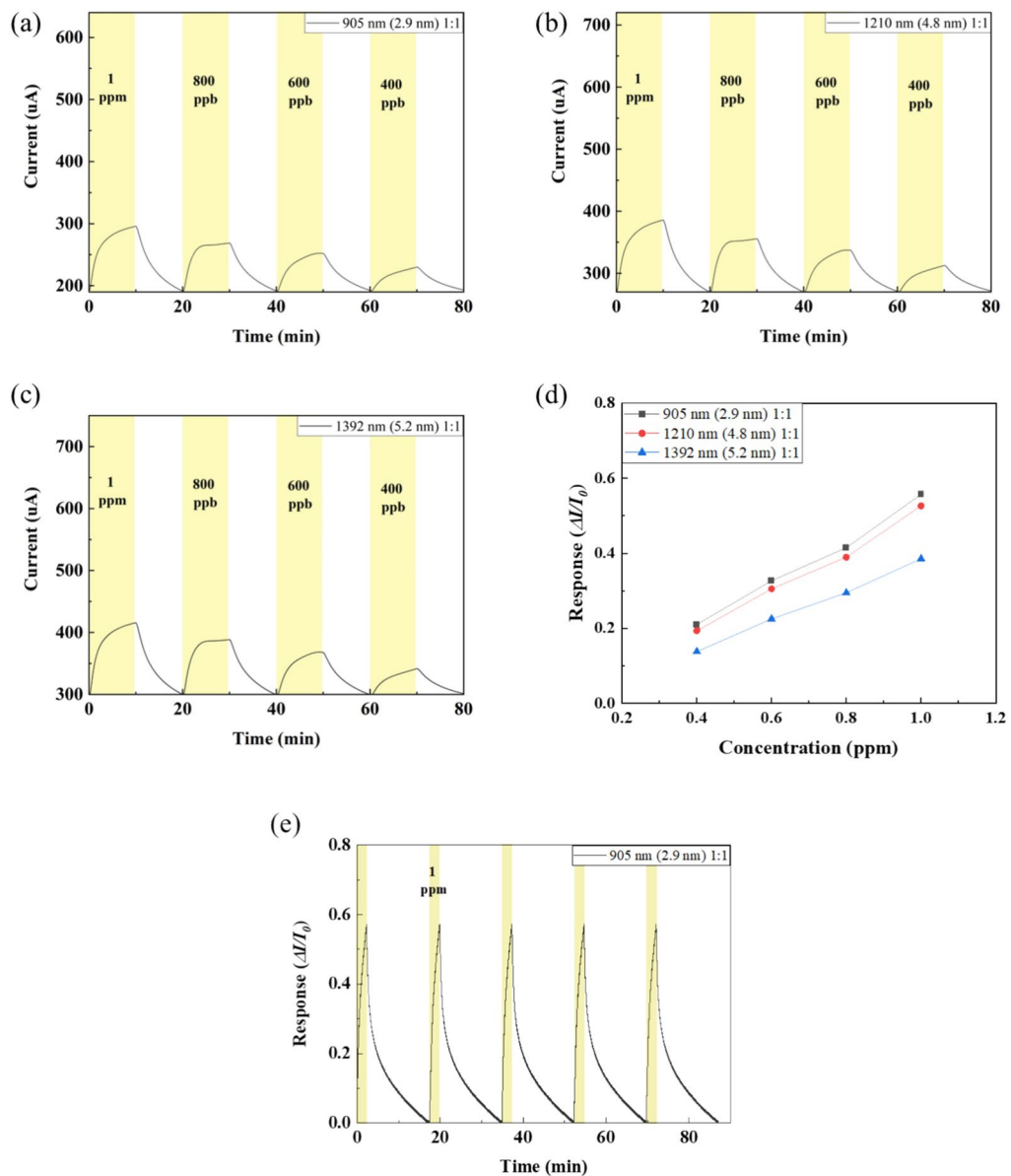


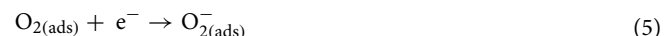
**Fig. 8.** (a–d) Current characteristics depending on the size of PbS QDs at the  $\text{NO}_2$  gas concentrations of 1–0.2 ppm, and (e) repeatability characteristics of the 2.9-nm PbS QD-based sensor at 25 °C.

concentration in real time, but also improve air pollution problems through a direct monitoring system at  $\text{NO}_2$  emission sources such as power plants, factories, and automobile exhaust.

Furthermore, to confirm the operation characteristics at high temperatures, the reactivity of the sensor toward 20–1-ppm  $\text{NO}_2$  gas was tested at 25 °C (room temperature), 50 °C, 100 °C, and 150 °C.

As demonstrated in Fig. 9, there is negligible difference in the responsivity values obtained at 50 °C and room temperature which is considered erroneous. The response at 100 °C is approximately 4 times higher than that obtained at room temperature, and the responsivity of  $\text{NO}_2$  gas and PbS QDs increases with increasing temperature. This is because  $\text{H}_2\text{O}$  evaporates at 100 °C, the number of sites that can react on the sensor surface increases, and physical oxygen adsorption occurs more easily on the surface, and the responsivity increases accordingly.

Before  $\text{NO}_2$  exposure, oxygen molecules in the air attach to the surface of PbS QDs and capture electrons to form  $\text{O}_2^-$  below 100 °C, or  $\text{O}^-$  between 100 and 150 °C creating a surface state similar to that of an acceptor<sup>33,37</sup>. The as-formed surface state causes the excitation of the electrons in the valence band and induces the formation of numerous holes in the p-type PbS QDs, creating an electron depletion layer near the surface.



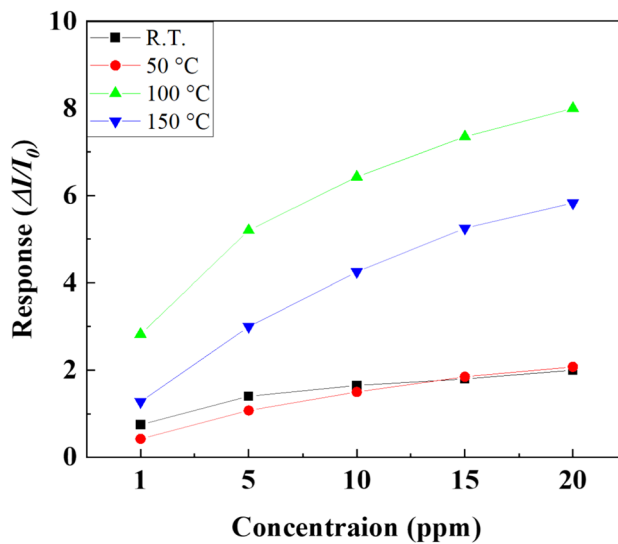


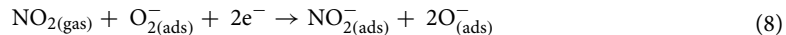
**Fig. 9.** Response characteristics of the fabricated sensor according to temperature conditions (20–1 ppm of  $\text{NO}_2$  gas).

Sensing material	Fabrication method	Temp	Concentration range	Response	LO	References
PbS films	Bath growing	RT	5–100 ppm	0.5	–	<sup>29</sup>
PbS NPs	SILAR technique	RT	10–100 ppm	0.1	–	<sup>30</sup>
PbS CQDs	Drop casting	RT	2.8–100 ppm	0.21	0.15 ppb	<sup>10</sup>
$\text{MoS}_2/\text{PbS}$ CQDs	Hydrothermal & Drop casting	RT	5–400 ppm	0.11	–	<sup>31</sup>
$\text{MoS}_2/\text{PbS}$ CQDs	Hydrothermal & Spin coating	RT	1–20 ppm	6.1	94 ppb	<sup>32</sup>
PbS films	PLD	150 °C	10–70 ppm	0.1	84 ppb	<sup>33</sup>
$\text{MoS}_2@\text{MoO}_3$	PVD	125 °C	0.5–10 ppm	0.3	150 ppb	<sup>34</sup>
$\text{In}_2\text{O}_3$ -graphene-Cu	Sol-gel & Drop casting	420 °C	7–20 ppm	1.66	–	<sup>35</sup>
MOF $\text{In}_2\text{O}_3$	Hydrothermal & Calcination	RT	1–1000 ppb	1210 (200 ppb)	1 ppb	<sup>36</sup>
P3HT/PbS CQDs	Sol-gel & Spin coating	RT	0.4–100 ppm	2.17	70 ppb	This work

**Table 1.** Recent reported researches of the  $\text{NO}_2$  gas sensor.



When exposed to  $\text{NO}_2$  gas, the oxidizing gas acts as an electron acceptor, and a reaction occurs on the PbS surface according to the following equations.



$\text{NO}_2$  molecules are directly adsorbed and acquire electrons from the PbS QD surface. Consequently, the hole concentration increases, whereas the depth of the electron depletion layer and height of the potential barrier decrease because of the oxidizing nature of  $\text{NO}_2$  and its substantially higher electron affinity than oxygen. Therefore, the sensor resistance decreases, and the current increases<sup>10,29–38</sup>. Additionally, owing to the high hole mobility of P3HT, the sensor response can be enhanced by improving the flow of charges<sup>18,19</sup>. The principle of  $\text{NO}_2$  gas detection is illustrated in Fig. 10.

At 150 °C, the response is reduced compared with that at 100 °C, which is considered to be because of the deterioration of the PbS QDs thin film. Therefore, the fabricated sensor can detect  $\text{NO}_2$  gas with high sensitivity even at temperatures up to 150 °C. Since most metal oxide-based gas sensors cannot react with oxygen in the air at low temperatures, they cannot form a site for reacting with the target gas in the material. Therefore, physical adsorption, which is a direct charge transfer between the sensing material and the target gas, is dominant. However, according to the reference, PbS QDs form a reaction site and have high reactivity due to relatively high

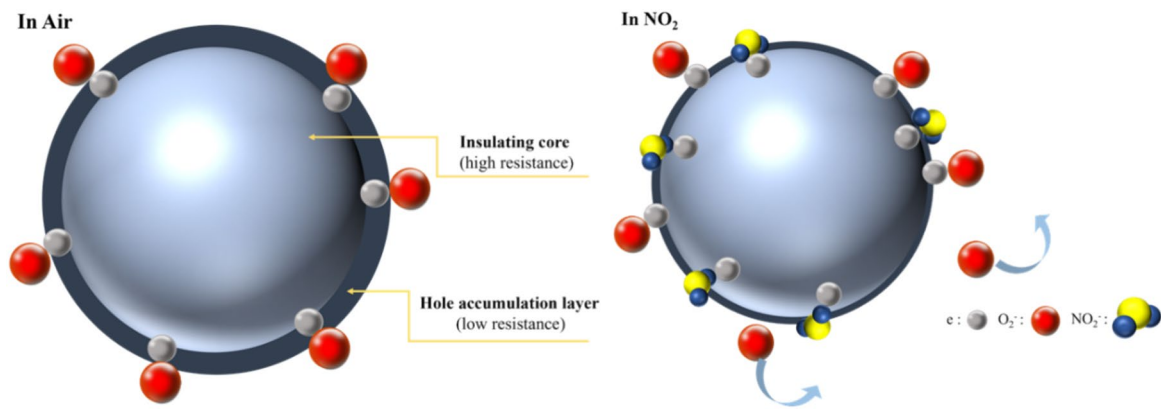


**Fig. 10.** Mechanism of  $\text{NO}_2$  gas sensing by PbS QDs.

binding energy to oxygen (0.5 eV) and  $\text{NO}_2$  (0.8 eV) even below 100 °C<sup>39</sup>. Because most metal oxide-based gas sensors require high temperatures above 300 °C for successful detection, PbS QDs-based gas sensors have the advantage of being able to operate at room temperature.

One issue with this sensor has observed that the properties of the sensing material deteriorated at high temperatures. In this manuscript, experimental measurements were not conducted at temperatures above 200 °C because the PbS QDs thin film was observed to be damaged by high temperature. This phenomenon is a major obstacle to commercialization. One possible way to resolve this issue is to form a polymer film on the surface of the sensing material which served as protective layer from the heat<sup>40,41</sup>. It was observed that the porosity of film can allow the gas to react with the sensing material, and greatly buffers the damage caused by high temperatures. The new findings will be reported shortly.

Additionally, to confirm the selectivity of the  $\text{NO}_2$  gas sensor fabricated using P3HT-doped PbS QDs, its reactivity to other gases was measured. The experiment was performed using 100 ppm of  $\text{CO}_2$ ,  $\text{H}_2\text{S}$ ,  $\text{CO}$ ,  $\text{CH}_4$  and  $\text{SO}_2$  gases for 10 min, and the measured results were compared with those obtained with 100 ppm of  $\text{NO}_2$  gas. As demonstrated in Fig. 11, although certain reactivity toward other gases is observed, it is negligible at a level of up to 7% compared with that toward  $\text{NO}_2$  gas<sup>10,28,31</sup>. In addition, to confirm the long-term stability of the fabricated sensor, the responsivity to 100 ppm  $\text{NO}_2$  gas was measured at 30 cycles every 5 days for a month. As can be seen in Fig. 12, it was confirmed that stable characteristics were maintained within the 3% error range caused by the measurement system and the measurement environment. Furthermore, the response of the fabricated PbS QD-based  $\text{NO}_2$  gas sensor to humidity was measured at 25 °C. The relative humidity of the environment was set to 30%, 60%, and 90% with a stabilization time of 20 min, and thereafter, the measurement was performed using 20 ppm  $\text{NO}_2$ . Humidity was controlled through the humidity generator of the MFC, and the humidity in the chamber was measured using a humidity sensor (RH-BTA, Vernier Software & technology). As the humidity increased, the resistance increased, whereas the initial current gradually decreased. Additionally, noise was generated owing to the presence of moisture. As presented in Fig. 13, the response values are 2.13, 1.89, and 1.79 at 30%, 60%, and 90% humidity, respectively, and the number of binding sites of  $\text{NO}_2$  decreased because of the

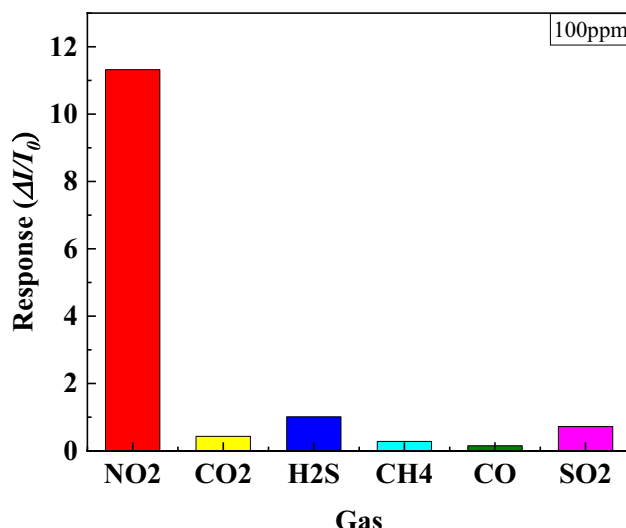


**Fig. 11.** Selectivity characteristics of the fabricated sensor according to the gas type.

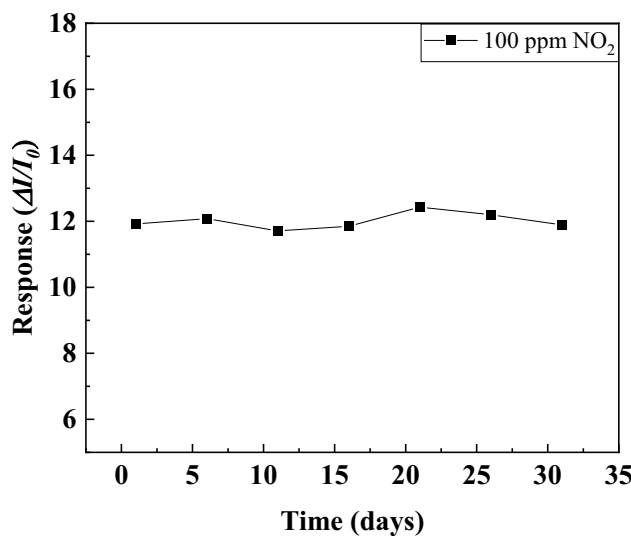


**Fig. 12.** Long-term reliability test of the fabricated sensor.

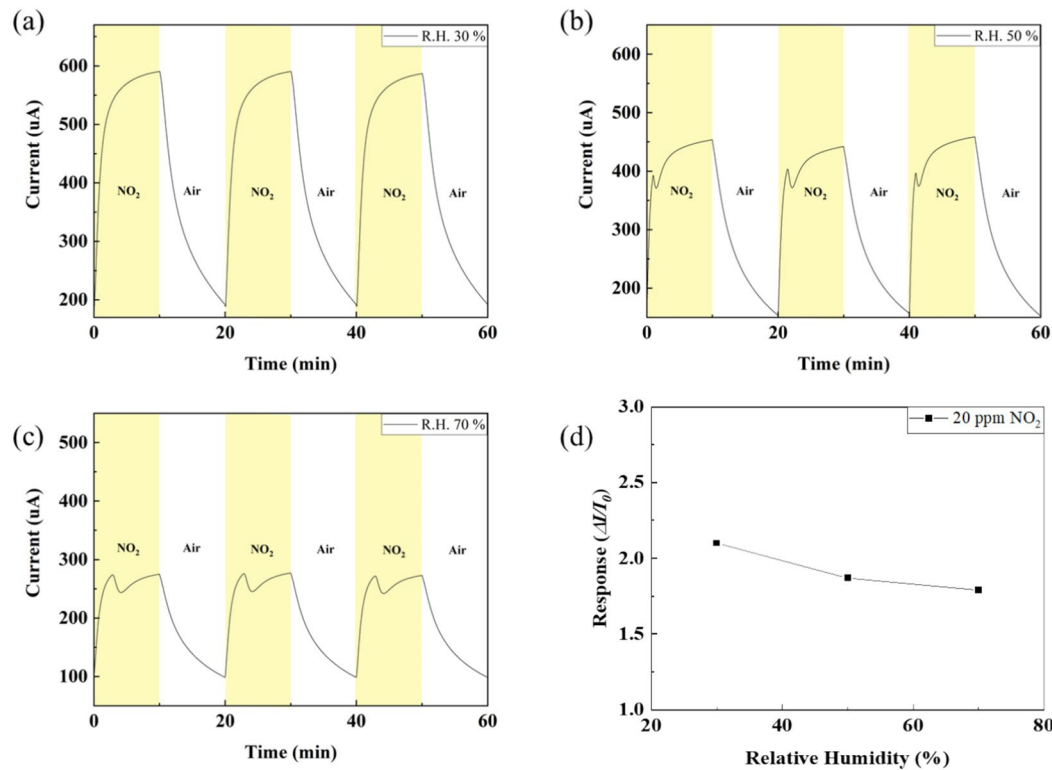


**Fig. 13.** Changes in (a–c) current and (d) response of the fabricated  $\text{NO}_2$  gas sensor depending on humidity variations (20-ppm  $\text{NO}_2$ ; 25 °C).

presence of moisture. However, this difference can be mitigated through packaging, and the fabricated sensor can be stably operated irrespective of the changes in season and weather.

## Conclusions

Herein, we developed a facile and high-sensitivity  $\text{NO}_2$  gas sensor based on PbS QDs for room-temperature detection. The synthesized PbS QDs were doped with P3HT to enhance the sensitivity and facile formation of the thin film for the  $\text{NO}_2$  gas sensor. Thereafter, the devices were fabricated by spin casting P3HT-doped PbS QDs onto IDE gold contacts on a  $\text{SiO}_2/\text{Si}$  substrate. The developed sensor could selectively detect  $\text{NO}_2$  gas with

high sensitivity owing to the high binding energy between PbS QDs and  $\text{NO}_2$  gas. Furthermore, because of P3HT doping, the quality and hole mobility of the thin film improved, resulting in high sensitivity. The device exhibits high sensitivity and selectivity toward  $\text{NO}_2$  gas and can exclusively detect  $\text{NO}_2$  among other air pollutants, such as  $\text{CH}_4$ ,  $\text{CO}$ , and  $\text{CO}_2$ . Moreover, it can detect 20–0.4-ppm  $\text{NO}_2$  gas with a resolution of 200 ppb. Herein, the highest responsivity was obtained under the conditions of a PbS QDs:P3HT ratio of 1:1, PbS QD size of approximately 2.9 nm, and PbS QDs absorption wavelength of 905 nm owing to the large surface area of the thin film. Compared with the state-of-the-art  $\text{NO}_2$  sensors, the as-developed sensor can detect  $\text{NO}_2$  gas with high sensitivity through the facile formation of a single thin film.

The proposed  $\text{NO}_2$  gas sensor demonstrates significant research interest and practical application potential as a highly selective sensing device for gases with diverse chemical properties. Furthermore, the versatility of the sensor material allows for its application on various substrates, including flexible ones. This adaptability enables direct installation on personnel in fossil fuel-based power plants and industrial facilities, thereby enhancing worker safety. However, it is widely known that QDs suffer from thermal stability<sup>42–44</sup>, and further research is being conducted to solve this problem. Improving the low thermal stability of PbS QDs is essential to secure stable operation characteristics of the sensor. Therefore, follow-up researches are continuously being conducted on improving thermal stability through passivation or ligand exchange of PbS QDs, and these studies will greatly contribute to the expansion of sensors into more harsh fields. The results will be submitted to the journal soon.

## Data availability

The data that support the findings of this study are available from the corresponding author upon reasonable request.

Received: 19 October 2023; Accepted: 28 August 2024

Published online: 04 September 2024

## References

1. Horowitz, C. Paris agreement. *Int. Leg. Mater.* **55**, 740–755 (2017).
2. Yan, W. *et al.*  $\text{NO}_2$  inhalation promotes Alzheimer's disease-like progression: Cyclooxygenase-2-derived prostaglandin E2 modulation and monoacylglycerol lipase inhibition-targeted medication. *Sci. Rep.* **6**, 22429–22445 (2016).
3. Gawali, S. R. *et al.* Ce doped NiO nanoparticles as selective  $\text{NO}_2$  gas sensor. *J. Phys. Chem. Solids* **114**, 28–35 (2018).
4. Shishiyaru, S. T. *et al.* Sensing characteristics of Tin-doped ZnO thin films as  $\text{NO}_2$  gas sensor. *Sens. Actuators B Chem.* **107**, 379–386 (2005).
5. Sonker, R. K. *et al.* Experimental investigations on  $\text{NO}_2$  sensing of Pure ZnO and PANI-ZnO composite thin films. *Mater. Lett.* **152**, 56149–56158 (2016).
6. Hotovy, I. *et al.* Sensing characteristics of NiO thin films as  $\text{NO}_2$  gas sensor. *Thin Solid Films* **418**, 9–15 (2002).
7. Shendage, S. S. *et al.* Sensitive and selective  $\text{NO}_2$  gas sensor based on  $\text{WO}_3$  nanoplates. *Sens. Actuators B* **240**, 426–433 (2017).
8. Li, M. Sensitive  $\text{NO}_2$  gas sensors employing spray-coated colloidal quantum dots. *Thin Solid Films* **618**, 271–276 (2016).
9. Liu, J. *et al.*  $\text{MoS}_2$  Nanosheets sensitized with quantum dots for room-temperature gas sensors. *Nanomicro Lett.* **12**, 59–71 (2020).
10. Mitri, F. *et al.* Lead sulphide colloidal quantum dots for room temperature  $\text{NO}_2$  gas sensors. *Sci. Rep.* **10**, 12556–12564 (2020).
11. Liu, Y. *et al.* Highly sensitive and selective ammonia gas sensors based on PbS quantum dots/ $\text{TiO}_2$  nanotube arrays at room temperature. *Sens. Actuators B* **236**, 529–536 (2016).
12. Kwon, J. B. *et al.* Air-stable and ultrasensitive solution-cast SWIR photodetectors utilizing modified core/shell colloidal quantum dots. *Nano Converg.* **7**, 1–10 (2020).
13. Kwon, J. B. *et al.* Brightness-enhanced, highly stable quantum dot light-emitting devices using butylated hydroxytoluene. *Org. Electron.* **74**, 166–171 (2019).
14. Kim, S. W. *et al.* An organic/inorganic nanomaterial and nanocrystal quantum dots-based multi-level resistive memory device. *Nanomaterials* **11**, 3004–3014 (2021).
15. Kim, S. W. *et al.* Stable hybrid organic/inorganic multiple-read quantum-dot memory device based on a PVK/QDs solution. *Appl. Surf. Sci.* **1**, 25–32 (2019).
16. Sonar, P. *et al.* Comparative behavior of CdS and CdSe quantum dots in poly(3-hexylthiophene) based nanocomposites. *Mater. Res. Bull.* **41**, 198–208 (2006).
17. Gemayel, M. E. *et al.* Graphene nanoribbon blends with P3HT for organic electronics. *Nanoscale* **6**, 6301–6314 (2006).
18. Seidler, N. *et al.* Enhanced crystallinity and film retention of P3HT thin-films for efficient organic solar cells by use of preformed nanofibers in solution. *J. Mater. Chem.* **1**, 7748–7757 (2013).
19. Jin, S. H. *et al.* Optimization of process parameters for high-efficiency polymer photovoltaic devices based on P3HT:PCBM system. *Sol. Energy Mater. Sol. Cells* **91**, 1187–1193 (2017).
20. Moreels, I. *et al.* Size-dependent optical properties of colloidal PbS quantum dots. *ACS Nano* **3**, 3023–3030 (2009).
21. Zhao, H. *et al.* Towards controlled synthesis and better understanding of highly luminescent PbS/CdS core/shell quantum dots. *J. Mater. Chem.* **21**, 8904–8988 (2011).
22. Sargent, E. H. Size-tunable infrared (1000–1600 nm) electroluminescence from solution-processable PbS quantum dot nanocrystals: Towards monolithic optoelectronic integration on silicon. *J. Mod. Opt.* **51**, 2797–2803 (2004).
23. Yang, X. *et al.* Iodide capped PbS/CdS core-shell quantum dots for efficient long-wavelength near-infrared light-emitting diodes. *Sci. Rep.* **7**, 14741–14746 (2017).
24. Nam, M. W. *et al.* Removing surface organic ligands and configuring a bilayer heterojunction with a new conjugated polymer. *Org. Electron. Phys. Mater. Appl.* **15**, 391–398 (2014).
25. Nam, M. W. *et al.* Broadband-absorbing hybrid solar cells with efficiency greater than 3% based on a bulk heterojunction of PbS quantum dots and a low-bandgap polymer. *J. Mater. Chem.* **2**, 3978–3985 (2014).
26. Gao, J. *et al.* Improvement in carrier transport properties by mild thermal annealing of PbS quantum dot solar cells. *Appl. Phys. Lett.* **102**, 43509–43510 (2013).
27. Kruefu, V. *et al.* C<sub>2</sub>H<sub>5</sub>OH gas sensing based on Poly(3-hexylthiophene)/Nb-Loaded ZnO nanocomposite films. *Mol. Cryst. Liq. Cryst.* **599**, 1–7 (2014).
28. Kwon, J. B. *et al.* Uncooled short-wave infrared sensor based on PbS quantum dots using ZnO NPs. *Nanomaterials* **9**, 926–934 (2019).
29. Zhang, F. *et al.* A flexible and wearable  $\text{NO}_2$  gas detection and early warning device based on a spraying process and an interdigital electrode at room temperature. *Microsyst. Nanoeng.* **8**, 40–49 (2015).

30. Burungale, V. V. *et al.* Chemically synthesized PbS nanoparticulate thin films for a rapid NO<sub>2</sub> gas sensor. *Mater. Sci. Pol.* **34**, 204–211 (2016).
31. Xin, X. *et al.* Enhanced performances of PbS quantum-dots-modified MoS<sub>2</sub> composite for NO<sub>2</sub> detection at room temperature. *ACS Appl. Mater. Interfaces* **11**, 9438–9447 (2019).
32. Liu, J. *et al.* MoS<sub>2</sub> nanosheets sensitized with quantum dots for room-temperature gas sensors. *Nano-Micro Lett.* **12**, 59–71 (2020).
33. Dawood, Y. Z. A study of the optical and structural properties of the PbS films that affect the sensitivity of the NO<sub>2</sub> gas sensor. *J. Opt.* **1**, 1–8 (2023).
34. Li, W. *et al.* Highly sensitive NO<sub>2</sub> gas sensors based on MoS<sub>2</sub>@MoO<sub>3</sub> magnetic heterostructure. *Nanomaterials* **12**, 1303–1319 (2023).
35. Khort, A. *et al.* High-performance selective NO<sub>2</sub> gas sensor based on In<sub>2</sub>O<sub>3</sub>-graphene-Cu nanocomposites. *Sci. Rep.* **13**, 7834–7845 (2023).
36. Han, J. *et al.* Interface-engineering in MOF-derived In<sub>2</sub>O<sub>3</sub> for highly sensitive and dual-functional gas sensor towards NO<sub>2</sub> and triethylamine. *Sens. Actuators B* **395**, 134491–134500 (2023).
37. Zhang, F. *et al.* A flexible and wearable NO<sub>2</sub> gas detection and early warning device based on a spraying process and an interdigital electrode at room temperature. *Microsyst. Nanoeng.* **8**, 40–49 (2022).
38. Li, M. *et al.* PbSe quantum dots-based chemiresistors for room-temperature NO<sub>2</sub> detection. *Sens. Actuators B* **256**, 1045–1056 (2016).
39. Liu, H. *et al.* Physically flexible, rapid-response gas sensor based on colloidal quantum dot solids. *Adv. Mater.* **26**, 2718–2724 (2014).
40. Ko, J. *et al.* Chemically resistant and thermally stable quantum dots prepared by shell encapsulation with cross-linkable block copolymer ligands. *NPG Asia Mater.* **12**, 19–29 (2020).
41. Kim, D. *et al.* Poly(methylmethacrylate) coating on quantum dot surfaces via photo-chemical reaction for defect passivation. *J. Photochem. Photobiol. A* **376**, 206–211 (2019).
42. Zhao, Y. *et al.* High-temperature luminescence quenching of colloidal quantum dots. *ACS Nano* **6**, 9058–9067 (2012).
43. Zheng, J. *et al.* Temperature-dependent photoluminescence properties of Mn:ZnCdS quantum dots. *RCS Adv.* **4**, 30948–30952 (2014).
44. Li, B. Revealing mechanisms of PL properties at high and low temperature regimes in CdSe/ZnS core/shell quantum dots. *J. Appl. Phys.* **124**, 44302–44307 (2018).

## Acknowledgements

This study has been conducted with the support of the Korea Institute of Industrial Technology as “Development and commercialization for clean hydrogen production/storage and CO<sub>2</sub> monitoring system in the field of industrial complex (Kitech EH-24-0007)”. This work was supported by the Korea Innovation Foundation(INNOPOLIS) grant funded by the Korea government(MSIT) (2020-DD-UP-0348). This research was financially supported by the Ministry of Small and Medium-sized Enterprises(SMEs) and Startups(MSS), Korea, under the “Regional Specialized Industry Development Plus Program(R&D, S3366018)” supervised by the Korea Technology and Information Promotion Agency for SMEs.

## Author contributions

J.B. and Y.T. H.K. conceived the basic idea and designed the devices and the experiments. Y.T. and S.J. prepared the QDs solutions and fabricated the devices. J.B. and S.J performed the device characterization. J.B., D.G. S.H. and D.W. analyzed and discussed the results. All authors revised the manuscript.

## Competing interests

The authors declare no competing interests.

## Additional information

**Correspondence** and requests for materials should be addressed to S.H.K. or D.J.

**Reprints and permissions information** is available at [www.nature.com/reprints](http://www.nature.com/reprints).

**Publisher's note** Springer Nature remains neutral with regard to jurisdictional claims in published maps and institutional affiliations.

**Open Access** This article is licensed under a Creative Commons Attribution-NonCommercial-NoDerivatives 4.0 International License, which permits any non-commercial use, sharing, distribution and reproduction in any medium or format, as long as you give appropriate credit to the original author(s) and the source, provide a link to the Creative Commons licence, and indicate if you modified the licensed material. You do not have permission under this licence to share adapted material derived from this article or parts of it. The images or other third party material in this article are included in the article's Creative Commons licence, unless indicated otherwise in a credit line to the material. If material is not included in the article's Creative Commons licence and your intended use is not permitted by statutory regulation or exceeds the permitted use, you will need to obtain permission directly from the copyright holder. To view a copy of this licence, visit <http://creativecommons.org/licenses/by-nc-nd/4.0/>.

© The Author(s) 2024